



Cite this: DOI: 10.1039/d1cy00278c

Preparation of a ZnIn₂S₄-ZnAlO_x nanocomposite for photoreduction of CO₂ to CO†

Yuqing Shao,^a Xinkui Wang,^a *^a Zhaolin Dou,^b Xiaoyu Liang,^a Xinxin Zhang,^a Min Pang,^c Qiang Xu,^a Min Ji ^a and Min Wang ^{*b}

Solar-driven CO₂ conversion into fuels and sustainable energy has attracted increasing attention around the world. However, the efficiency of the transformation remains relatively low due to the rapid recombination of photogenerated charge carriers. In this work, we prepared a ZnIn₂S₄-ZnAlO_x nanocomposite for visible light driven CO₂ reduction. The thin layered structure facilitated the photoinduced charge carrier separation and transfer, and also gave excellent adsorption ability towards CO₂ molecules. Such a nanocatalyst exhibited excellent activity in visible-light driven CO₂ reduction with a CO optimal formation rate of 1100 μmol g⁻¹ h⁻¹, which is 5 times that over bulk ZnIn₂S₄, and the CO/H₂ ratio was increased from 0.2 over bulk ZnIn₂S₄ to 1.5 over the ZnIn₂S₄-ZnAlO_x composite. *In situ* FT-IR experiments indicated that CO₂ was reduced on ZnIn₂S₄-ZnAlO_x following a COOH* pathway. This work gives insights into the mechanism of the photocatalytic CO₂ reduction reaction and inspiration to construct novel heterostructure materials for application in energy and environmental catalysis.

Received 13th February 2021,
Accepted 28th March 2021

DOI: 10.1039/d1cy00278c

rsc.li/catalysis

Introduction

The conversion of CO₂ into chemicals and fuels has aroused worldwide interest, and solar-driven CO₂ reduction is a promising route and has attracted increasing attention.¹⁻⁶ During the past few decades, great efforts have been devoted to developing various photocatalysts with different structures for efficient CO₂ photoreduction.⁷⁻⁹ However, the unsatisfactory separation efficiency of photogenerated charge carriers is one of the most critical issues that remarkably restricts the performance of semiconductor photocatalysts.¹⁰⁻¹³ During the photocatalytic process, photoinduced carriers, electrons (e⁻) and holes (h⁺), recombined much faster than their migration from the bulk to the surface, therefore resulting in low efficiency.^{14,15} To overcome these drawbacks, various strategies have been developed to inhibit the recombination of photogenerated holes and electrons, such as the construction of

heterojunctions, heterophase junctions, and thin layer structures.¹⁶⁻¹⁸ It is found that decreasing the thickness of materials can shorten the photoinduced carrier transfer distance to the surface and thus inhibits their recombination in the bulk phase. Construction of a thin layer two-dimensional structure is an efficient way to promote the efficiency of CO₂ photoreduction.

ZnIn₂S₄ is a visible light responsive semiconductor with a conduction band of -1.0 eV, and could be used as a photocatalyst for CO₂ reduction under visible light. Bulk ZnIn₂S₄ itself showed low activity due to easy recombination of holes and electrons in the bulk.¹⁹ The construction of ZnIn₂S₄@CNO and the ZnIn₂S₄-In₂O₃ composite promoted the carrier separation and increased the activity, but needs Co(bpy)₃²⁺ as a cocatalyst.^{20,21} Recently, immobilization of CeO₂ on ZnIn₂S₄ increased the CO generation rate from 95 to 180 μmol g⁻¹ h⁻¹, but hydrogen is more easily produced with a CO/H₂ ratio of about 0.3, lowering the quantum yield.²²

In this paper, we report a ZnIn₂S₄-ZnAlO_x nanocomposite for the photocatalytic reduction of CO₂ to CO. ZnAlO_x was used to exfoliate and stabilize a ZnIn₂S₄ nanosheet. A thin layer of ZnIn₂S₄ was *in situ* grown on ZnAlO_x. Moreover, the ZnAlO_x material gives abundant active sites for CO₂ adsorption. This ZnIn₂S₄-ZnAlO_x nanocomposite reduced the bulk-to-face diffusion length to accelerate the separation of charge carriers and favor CO₂ adsorption, therefore facilitating the conversion of CO₂ to CO, and suppressed hydrogen generation. The optimal yield of CO over ZnIn₂S₄-

^a State Key Laboratory of Fine Chemicals, School of Chemical Engineering, Dalian University of Technology, Dalian 116024, China. E-mail: wangxinkui@dlut.edu.cn

^b Zhang Dayu School of Chemistry, Dalian University of Technology, Dalian 116024, China. E-mail: wangmin@dlut.edu.cn

^c Institute of Materials, China Academy of Engineering Physics, Mianyang 621907, China

† Electronic supplementary information (ESI) available. See DOI: 10.1039/d1cy00278c

ZnAlO_x reaches up to 1100.5 μmol g⁻¹ h⁻¹, which is 5 times that over bulk ZnIn₂S₄, and the CO/H₂ ratio was increased from 0.2 over bulk ZnIn₂S₄ to 1.5 over the ZnIn₂S₄-ZnAlO_x composite.

Results and discussion

General characterization of the catalysts

The ZnIn₂S₄-ZnAlO_x nanocomposite was prepared *via in situ* growth on ZnAlO_x. The XRD results showed that several phases exist in the ZnAlO_x sample, including Zn(OH)₂, AlOOH, ZnAl₂O₄ and Zn₃(OH)₄(NO₃)₂. As shown in Fig. S1† the peak at 36.8° can be attributed to the ZnAl₂O₄ phase (JCPDS card No. 05-0669). The peaks at 19.4°, 32.8° and 61.9° corresponded to (001), (100) and (111) facets of Zn(OH)₂, respectively (JCPDS card No. 24-1444). The peaks at 28.8°, 38.5°, 42.7° and 69.8° corresponded to the (110), (200), (111) and (130) facets of AlOOH, respectively (JCPDS card No. 54-0036). The peak at 12.8° can be attributed to Zn₃(OH)₄(NO₃)₂ (JCPDS card No. 52-0627). The (311) plane of cubic ZnAl₂O₄ and the (200) and (111) planes of AlOOH were observed in the TEM images (Fig. S2†).²³ ZnIn₂S₄ shows typical peaks at 20.5°, 27.4° and 47.4° (JCPDS card No. 72-0773). In the XRD pattern of ZnIn₂S₄-ZnAlO_x, there are three main peaks at 21.4°, 27.8° and 47.5°, which are assigned to the (006), (102) and (110) crystal facets of hexagonal ZnIn₂S₄, respectively. The growth of ZnIn₂S₄ on ZnAlO_x destroyed the crystal structure of ZnAlO_x probably because Zn on ZnAlO_x was involved in the growth of ZnIn₂S₄, indicating the strong interaction between ZnIn₂S₄ and ZnAlO_x. This interaction caused the shrinkage of the crystal cells as evidenced by the 2 theta value shift of the peaks to a higher angle. Besides, the FT-IR spectrum of ZnIn₂S₄-ZnAlO_x (Fig. S3†) shows a band at 1620 cm⁻¹, which was ascribed to the stretching vibrations of OH groups of adsorbed H₂O. NO₃⁻ from starting materials was introduced in ZnAlO_x as evidenced by the appearance of peaks at 1762, 1384 and 831 cm⁻¹.^{24,25} These bands vanished on the spectrum of ZnIn₂S₄-ZnAlO_x due to the separation of ZnAlO_x sheets from nitrates in the process of exfoliation.

The morphologies and microstructures of the composite were investigated by TEM and HAADF-STEM. From Fig. 1a and b, both TEM and STEM images show a network structure composed of multiple thin layers with a thickness of approximately 5 nm, rather than microspheres with a diameter on the μm scale, which is a typical structure of bulk ZnIn₂S₄ (Fig. S4†). According to Fig. 1c and d, the lattice distances of 0.31 and 0.46 nm were ascribed to the AlOOH (110) and Zn(OH)₂ (100) facet, 0.32 nm corresponded to the ZnIn₂S₄ (102) facet,²⁶ and 0.24 nm was ascribed to the ZnAl₂O₄ (311) facet, consistent with the XRD result in Fig. S1†. The EDX mapping images in Fig. 1(e) indicate the even dispersion of Zn, In, S, Al and O elements.

To unveil the elemental states and chemical properties of the samples, X-ray photoelectron spectroscopy (XPS) was employed on ZnIn₂S₄-ZnAlO_x and ZnIn₂S₄. From the survey spectrum in Fig. 2a, the spectrum of ZnIn₂S₄-ZnAlO_x shows

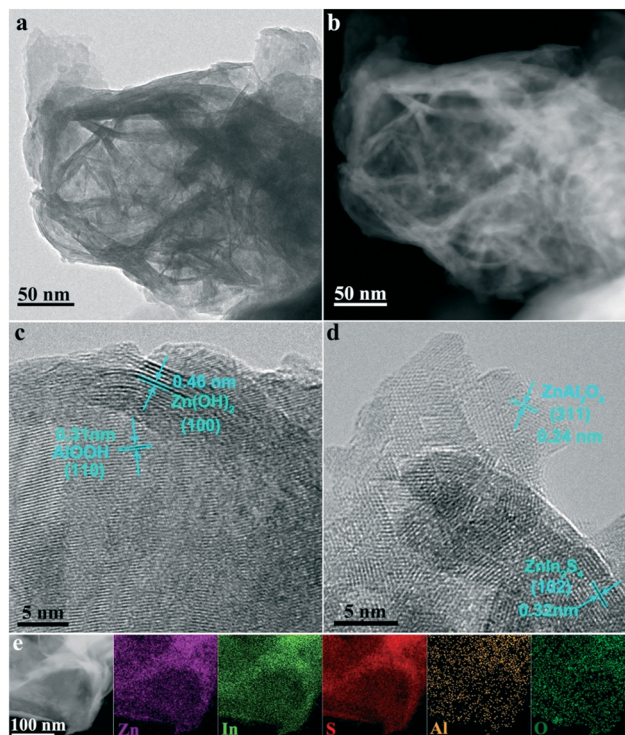


Fig. 1 (a) TEM, (b) HAADF-STEM, and (c and d) HRTEM images and (e) EDX mappings of Zn, In, S, Al, and O elements of ZnIn₂S₄-ZnAlO_x.

characteristic peaks of Zn, In, S, Al and O elements, which is consistent with the EDX elemental mapping analysis. As depicted in Fig. 2b, the binding energies of Zn 2p_{3/2} and Zn 2p_{1/2} for ZnIn₂S₄ were 1022.6 and 1046.2 eV, indicating that the chemical state of Zn was +2.²⁷ As for the In 3d spectrum, two peaks at 445.1 and 452.7 eV were ascribed to In 3d_{5/2} and In 3d_{3/2}, respectively.²⁸ The spectrum of S 2p can be fitted into two peaks centered at 161.6 and 162.7 eV, which are assigned to S²⁻.²⁹ However, the binding energies all shifted

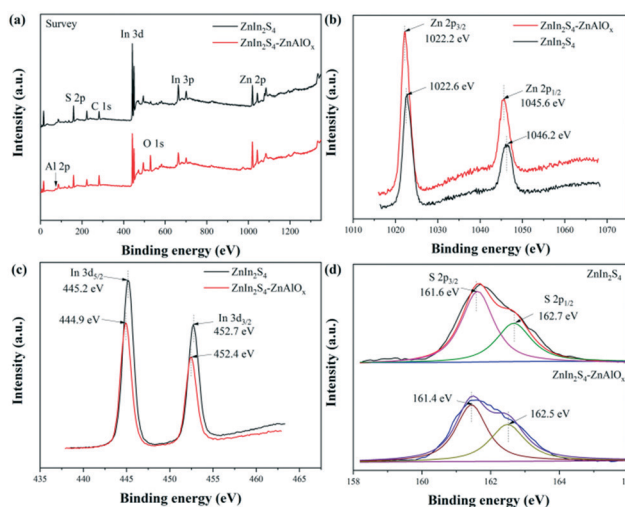


Fig. 2 (a) XPS survey spectra of ZnIn₂S₄-ZnAlO_x and ZnIn₂S₄ and (b-d) high-resolution spectra of Zn, In and S.

negatively after ZnIn_2S_4 and ZnAlO_x were combined. The Zn ($2p_{3/2}$: 1022.2 eV, $2p_{1/2}$: 1045.6 eV), In ($3d_{5/2}$: 444.9, $3d_{3/2}$: 452.4 eV) and S ($2p_{3/2}$: 161.4 eV, $2p_{1/2}$: 162.5 eV) binding energies of ZnIn_2S_4 - ZnAlO_x are 0.6, 0.3 and 0.2 eV lower than those of bulk ZnIn_2S_4 , respectively. The shift of Zn, In and S binding energies suggests the existence of intimate interfaces between ZnIn_2S_4 and ZnAlO_x , which is beneficial for fast separation and transportation of photo-induced charge carriers.³⁰

Photocatalytic CO_2 reduction performance

The CO_2 photoreduction reaction was carried out in an acetonitrile/ H_2O system with triethylamine (TEA) as the electron donor under atmospheric CO_2 and visible light (455 nm) irradiation. Fig. 3a shows the catalytic performance of ZnAlO_x and ZnIn_2S_4 - ZnAlO_x with different ZnIn_2S_4 contents. ZnAlO_x itself did not possess the ability to reduce CO_2 to CO. The highest CO yield (1100.5 μmol per gram ZnIn_2S_4 per hour) was obtained on the ZnIn_2S_4 - ZnAlO_x catalyst with 40 wt% content, while the H_2 yield was significantly suppressed as well. The H_2 yield on 60%- ZnIn_2S_4 - ZnAlO_x and 80%- ZnIn_2S_4 - ZnAlO_x was almost 2 and 3 times the CO yield, while the CO yield was over 1.5 times the H_2 yield on 40%- ZnIn_2S_4 - ZnAlO_x , which promoted the CO production and inhibited the competition hydrogen generation reaction. This is probably due to the beneficial effects of 40%- ZnIn_2S_4 - ZnAlO_x on the adsorption toward CO_2 molecules, which is studied by CO_2 adsorption FT-IR experiments in the following section. The control experiment using the physical mixture of ZnIn_2S_4

and ZnAlO_x shows a much lower CO yield, which further suggests the intimate and strong interaction between ZnIn_2S_4 and ZnAlO_x (Fig. 3b, column 1). When Ar was used instead of CO_2 , no CO was yielded, indicating that CO was formed by CO_2 reduction (Fig. 3b, column 2). Furthermore, when the experiment was carried out in the dark, the yield of CO and H_2 clearly decreased (Fig. 3b, column 3). In addition, when the experiment was conducted in the absence of a catalyst or TEA, no significant product was detected, which suggests the crucial role of TEA as an electron donor (Fig. 3b, column 4–5). The reaction can be carried out under UV-light illumination and the CO yield reaches above 10 000 $\mu\text{mol g}_{\text{ZnIn}_2\text{S}_4}^{-1} \text{h}^{-1}$ (Fig. 3b, column 6), which is in line with the stronger absorption in the UV-light region. This is further confirmed by the UV-vis DRS spectrum in the following section. The volume ratio of MeCN to H_2O was also investigated and the optimal ratio was determined to be 9 : 1, as shown in Fig. 3c. The decrease of water content would reduce the competitive reaction of hydrogen evolution and increase the CO/ H_2 ratio. Long-term experiments were carried out in the scale-up system, and 40%- ZnIn_2S_4 - ZnAlO_x showed durable photoreduction activity with an accumulated CO yield of 517.8 μmol . When the catalyst was used in stability tests, the yield of CO showed a slight decrease in each cycle (Fig. S5[†]), which is probably due to the photocorrosion of the ZnIn_2S_4 -based semiconductor catalyst.³¹ These results proved the excellent CO_2 photocatalytic activity of the ZnIn_2S_4 - ZnAlO_x nanocomposite, which is superior to those studied in the literature.^{32–34}

Optical and electrochemical performance

The UV-vis DRS method was adopted to give information on the optical properties and light absorption abilities of the samples. In Fig. 4a, ZnIn_2S_4 shows strong absorption of light with a steep decrease in the visible light region, while ZnAlO_x

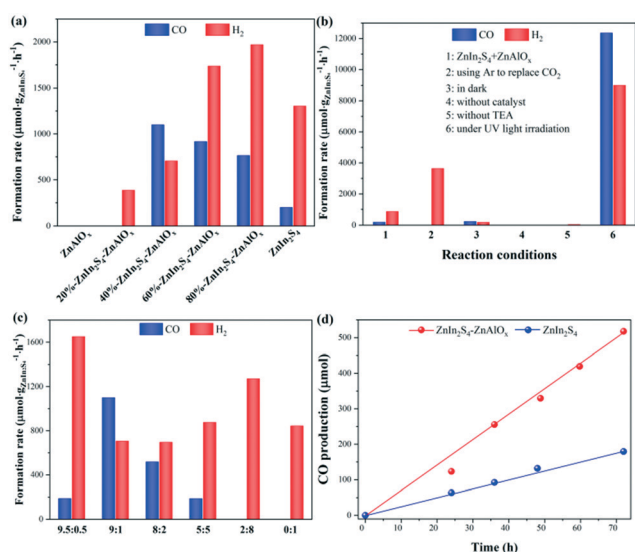


Fig. 3 (a) Catalyst screening, (b) control experiments over ZnIn_2S_4 - ZnAlO_x , (c) solvent effects on ZnIn_2S_4 - ZnAlO_x and (d) time course of ZnIn_2S_4 and ZnIn_2S_4 - ZnAlO_x . Reaction conditions: 5 mg of catalyst, 0.9 mL of MeCN, 0.1 mL of H_2O , 0.1 mL of triethylamine, 1 bar CO_2 , 9 W blue LEDs (455 nm), $\sim 25^\circ\text{C}$, 12 h. Scale-up reaction: 100 mg of catalyst, 18 mL of MeCN, 2 mL of H_2O , 2 mL of triethylamine, 1 bar of CO_2 , $\sim 42^\circ\text{C}$, 72 h.

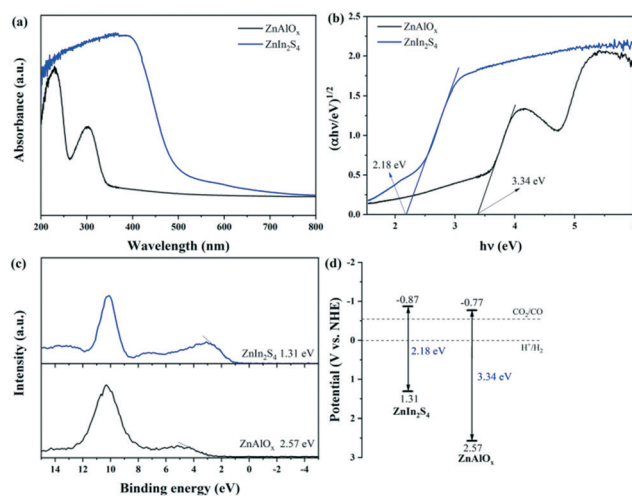


Fig. 4 (a) UV-vis diffuse reflectance spectra, (b) Tauc plots, (c) valence band XPS spectra and (d) band gap structures of ZnIn_2S_4 and ZnAlO_x .

only shows absorption in the UV light region with two absorption peaks at around 230 and 300 nm.³⁵ The band gap energies were calculated according to the Kubelka–Munk function ($\alpha h\nu = A(h\nu - E_g)^{n/2}$, where α , h , ν , E_g and A stand for the adsorption coefficient, Planck constant, light frequency, band gap energy and a constant, respectively, and n is 1 for the direct band gap semiconductor and 4 for the indirect band gap semiconductor). Fig. 4b presents the band gap energies of the two samples. The band gap energy of ZnIn₂S₄ (2.18 eV) is lower than that of ZnAlO_x (3.34 eV). The valence band XPS results in Fig. 4c indicate that the valence band of ZnIn₂S₄ (1.31 eV) is lower than that of ZnAlO_x (2.57 eV). According to the equation: $E_g = E_{VB} - E_{CB}$, the conduction band positions of ZnIn₂S₄ and ZnAlO_x were calculated to be -0.87 and -0.77 eV, respectively. Given the analysis above, the band structures of the samples are presented in Fig. 4d. The results indicate that ZnIn₂S₄ is the photoactive species under visible light irradiation and ZnAlO_x cannot be excited by visible light.

In order to investigate the chemical behavior of photogenerated electron–hole pairs, we conducted electrochemical tests on ZnIn₂S₄ and ZnIn₂S₄–ZnAlO_x. The transient photocurrent responses were recorded to study the behavior of photogenerated electron–hole pairs. As shown in Fig. 5a, ZnIn₂S₄–ZnAlO_x shows higher photocurrent density than bare ZnIn₂S₄, which suggests a more efficient separation of photoinduced electron–hole pairs. The separation–recombination of photogenerated charge carriers was studied by PL spectra (Fig. 5b). The strong emission at about 603 nm on the spectrum of ZnIn₂S₄ is produced by the recombination of photogenerated electron–hole pairs. However, the luminescence emission of ZnIn₂S₄–ZnAlO_x is weaker, indicating a more efficient separation of electron–hole pairs.³⁶

CO₂ adsorption properties

In order to further investigate the adsorption ability of the composite towards CO₂, we employed *in situ* CO₂ adsorption FT-IR on ZnIn₂S₄–ZnAlO_x. From Fig. 6, it can be noted that when CO₂ was not injected to the system, the background spectrum was a straight line. After the injection of pure CO₂ gas, several peaks were observed as the characteristic adsorption peaks of CO₂. The peaks at 1618 and 1359 cm⁻¹

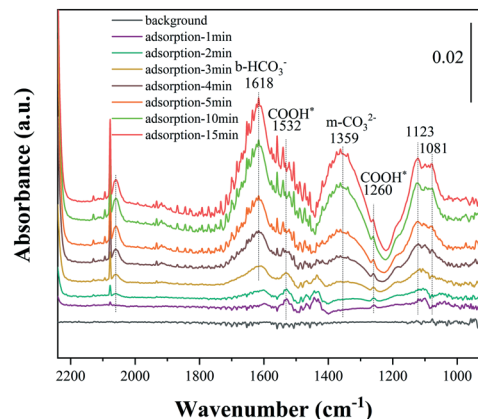


Fig. 6 *In situ* FT-IR spectra of ZnIn₂S₄–ZnAlO_x.

can be assigned to bidentate bicarbonate (b-HCO₃⁻) and bidentate carbonate (b-CO₃²⁻), respectively.²² The peaks at 1532 and 1260 cm⁻¹ can be ascribed to formate (COO⁻), which suggests that CO₂ reduction followed a COOH* pathway.^{37,38}

Conclusions

In summary, we synthesized a ZnIn₂S₄–ZnAlO_x thin-layer-structure nanocomposite for efficient visible-light driven CO₂ conversion to CO. TEM and XRD results indicate the successful combination of the ZnIn₂S₄ nanosheet and ZnAlO_x layer structure. ZnAlO_x was used to stabilize ZnIn₂S₄ for the adsorption of CO₂. Moreover, the ZnIn₂S₄–ZnAlO_x nanocomposite reduces the bulk-to-face diffusion path length, and therefore accelerating the separation of photoinduced charge carriers, which is proved by transient photocurrent responses and PL spectra. The formation rate of CO reaches up to 1100 μmol g⁻¹ h⁻¹ at ambient temperature and atmospheric CO₂ pressure. CO₂ adsorption FT-IR experiments revealed that the reaction followed a COOH* pathway. This work will provide insights into photocatalytic CO₂ reduction for wider applications in the photoreduction field.

Experimental

Materials

Zn(NO₃)₂·6H₂O (99.0%), ZnSO₄·7H₂O (99.5%), and hexamethylenetetramine (99.0%) were purchased from Tianjin Damao Corporation, Al(NO₃)₃·9H₂O (99.0%) was purchased from Aladdin Corporation, InCl₃·4H₂O (99.9%) was purchased from Energy Chemical, thioacetamide (TAA, 99%) was purchased from Macklin Reagent Company, isobutyl alcohol (99%) was obtained from Tianjin Kermel Chemical Reagent Development Center, China, and triethylamine (TEA, 99%) was purchased from Xilong Scientific Corporation. Deionized water used in all experiments was obtained from a Milli-Q system (Millipore). All reagents were used without further purification.

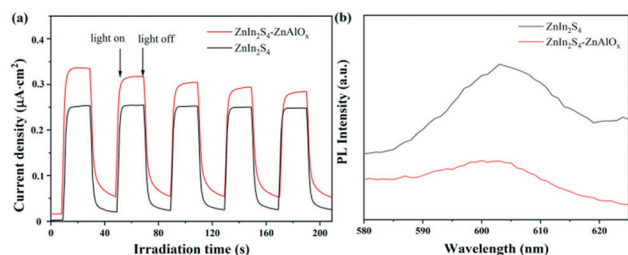


Fig. 5 (a) Transient photocurrent responses and (b) PL emission spectra of ZnIn₂S₄ and ZnIn₂S₄–ZnAlO_x; excitation wavelength: 400 nm.

Synthesis of ZnAlO_x

ZnAlO_x was prepared by a hexamethylenetetramine hydrolysis method according to the literature.³⁹ 0.20 mol Zn(NO₃)₂·6H₂O, 0.10 mol of Al(NO₃)₃·9H₂O and 0.26 mol of hexamethylenetetramine were dissolved in 200 mL deionized water, then placed into an autoclave with Teflon-lining, which then placed into an oven at 140 °C for 9 h. The product was centrifuged, washed thoroughly with deionized water, and dried at 60 °C overnight. The final product was labeled ZnAlO_x.

Synthesis of ZnIn₂S₄-ZnAlO_x

ZnIn₂S₄-ZnAlO_x was prepared with a hydrothermal method. Typically, 254.0 mg of as-prepared ZnAlO_x was dispersed in 30 mL isopropyl alcohol in a 100 mL beaker, followed by magnetic stirring for 2 h. Then 115.0 mg of ZnSO₄·7H₂O, 234.6 mg of InCl₃·4H₂O and 100 mg of cetyltrimethylammonium bromide (CTAB) were added to the above solution and stirred for 30 min followed by addition of an excess amount of thioacetamide (TAA) (180.3 mg). The mixture was stirred for another 30 min, and then transferred to a 100 mL stainless Teflon-lined autoclave, tightly sealed and placed in a 160 °C oven for 20 h. The autoclave was then naturally cooled to room temperature. The product was washed with absolute ethanol (3 × 40 mL) and deionized water (3 × 40 mL). After being dried in a vacuum at 60 °C for 12 h, a yellow solid was obtained as ZnIn₂S₄-ZnAlO_x.

General characterization

X-ray diffraction patterns (XRD) were obtained with a Smartlab 9 kW (Rigaku Corporation) diffractometer, using Cu-Kα radiation at 45 kV and 200 mA. High-angle annual dark-field scanning transmission electron microscopy (HAADF-STEM) images and energy dispersive spectroscopy (EDS) elemental mapping of the samples were recorded with a JEOL JEM-2100F microscope operated at 200 kV. X-ray photoelectron spectroscopy (XPS) and valence band XPS (VB-XPS) analysis were performed with an ESCALAB250Xi (Thermo, USA) using Al Kα (1486.6 eV) as the excitation source. The binding energies of Zn 2p, In 3d and S 2p were calibrated according to C 1s (284.6 eV). UV-vis diffuse reflectance spectra (UV-vis DRS) were recorded on a UV-vis spectrophotometer (Agilent UV-550) at room temperature in the range of 200–800 nm with BaSO₄ as the background. Photoluminescence (PL) emission spectra were obtained with a luminescence spectrometer from Hitachi F7000 at an excitation wavelength of 400 nm. Fourier transform infrared (FT-IR) spectroscopy and *in situ* Fourier transform infrared (*In situ* FT-IR) spectroscopy were conducted on a Nicolet iS10 IR spectrometer equipped with an MCT/A detector. For CO₂ adsorption, the samples were first treated in an FT-IR cell in a vacuum at 150 °C for 0.5 h then cooled to room temperature. After pretreatment, a background spectrum was recorded at a resolution of 4 cm⁻¹ and then subtracted automatically from the subsequent spectra. Each sample was

then exposed to pure CO₂ gas and adsorption spectra were recorded at intervals.

Electrochemical tests

The electrochemical tests were conducted on an electrochemical workstation (Corrtest CS2350H). A three-electrode system with a platinum-plate electrode as the counter electrode and a saturated calomel electrode (SCE) as the reference electrode was used for measurements. Na₂SO₄ (0.5 M) was used as the electrolyte solution. The working electrode is fluorine-tin oxide (FTO) coated with the sample (the slurry of the suspension: 10 mg mL⁻¹ concentration and ethanol/H₂O acts as a solvent).

Photocatalytic CO₂ reduction

The photocatalytic CO₂ reduction was performed in a home-built LED photoreactor. Typically, 5 mg of catalyst, 0.9 mL of acetonitrile (MeCN), 0.1 mL of H₂O and 0.1 mL of triethylamine (TEA) were added into a 6.5 mL quartz tube as a photoreactor. 9 W LEDs centered at 455 nm were used as light sources. Before irradiation, high purity CO₂ gas was introduced into the photoreactor for 30 s. During the photoreduction process, the reactants were magnetically stirred for 12 h and the temperature of the reaction system was kept at 25 °C. After the reaction, the gas sample was analyzed using a gas chromatograph (GC7890, Shanghai Tianmei Co., Ltd., China) equipped with a TDX-01 column and a thermal conductivity detector (TCD), and pure He was used as an internal standard. In a scale-up reaction, 100 mg of catalyst, 18 mL MeCN, 2 mL of H₂O and 2 mL of TEA were added into a 200 mL quartz photoreactor and a 300 W Xe lamp was used as a light source. Before irradiation, the reactor was purged with pure CO₂ gas five times. The pressure was kept at atmospheric pressure when the purge was finished. 5 mL of pure He was then injected to the system as an internal standard. After that, the light was switched on and the temperature of the system was kept below 42 °C. The gas product was taken and detected by GC at intervals.

Conflicts of interest

There are no conflicts to declare.

Acknowledgements

We are grateful for financial support from the National Natural Science Foundation of China (21978032, 21676045, 21770643, 21802131), the Natural Science Foundation of Liaoning Province (201602169) and the Fundamental Research Funds for the Central Universities (DUT18LK34, DUT19TD28).

References

- 1 Q. Wang, H. H. Tay, Z. Zhong, J. Luo and A. Borgna, *Energy Environ. Sci.*, 2012, 5, 7526–7530.

- 2 S. Wang, S. Yan, X. Ma and J. Gong, *Energy Environ. Sci.*, 2011, **4**, 3805–3819.
- 3 A. Goepfert, M. Czaun, J.-P. Jones, G. K. S. Prakash and G. A. Olah, *Chem. Soc. Rev.*, 2014, **43**, 7995–8048.
- 4 X. Chen, Z. Wang and D. D. Wu, *Hum. Ecol. Risk Assess.*, 2013, **19**, 1309–1323.
- 5 B. Yuan, X. Wu, Y. Chen, J. Huang, H. Luo and S. Deng, *Environ. Sci. Technol.*, 2013, **47**, 5474–5480.
- 6 X. X. Chang, T. Wang and J. L. Gong, *Energy Environ. Sci.*, 2016, **9**, 2177–2196.
- 7 H. L. Nguyen, *Adv. Energy Mater.*, 2020, **10**, 2002091.
- 8 H.-L. Wu, X.-B. Li, C.-H. Tung and L.-Z. Wu, *Adv. Mater.*, 2019, **31**, 1900709.
- 9 X. Li, J. Yu, M. Jaroniec and X. Chen, *Chem. Rev.*, 2019, **119**, 3962–4179.
- 10 M. Han, S. Zhu, S. Lu, Y. Song, T. Feng, S. Tao, J. Liu and B. Yang, *Nano Today*, 2018, **19**, 201–218.
- 11 C. N. C. Hitam, A. A. Jalil and A. A. Abdulrasheed, *J. Ind. Eng. Chem.*, 2019, **74**, 172–186.
- 12 C.-C. Wang, Y.-Q. Zhang, J. Li and P. Wang, *J. Mol. Struct.*, 2015, **1083**, 127–136.
- 13 P. D. Tran, L. H. Wong, J. Barber and J. S. C. Loo, *Energy Environ. Sci.*, 2012, **5**, 5902–5918.
- 14 J. Li, L. Cai, J. Shang, Y. Yu and L. Zhang, *Adv. Mater.*, 2016, **28**, 4059–4064.
- 15 J. Z. Zhang, *J. Phys. Chem. B*, 2000, **104**, 7239–7253.
- 16 M. F. R. Samsudin, H. Ullah, A. A. Tahir, X. Li, Y. H. Ng and S. Sufian, *J. Colloid Interface Sci.*, 2021, **586**, 785–796.
- 17 Z. Fang, S. Weng, X. Ye, W. Feng, Z. Zheng, M. Lu, S. Lin, X. Fu and P. Liu, *ACS Appl. Mater. Interfaces*, 2015, **7**, 13915–13924.
- 18 C. Du, Q. Zhang, Z. Lin, B. Yan, C. Xia and G. Yang, *Appl. Catal., B*, 2019, **248**, 193–201.
- 19 Y. Pan, X. Yuan, L. Jiang, H. Yu, J. Zhang, H. Wang, R. Guan and G. Zeng, *Chem. Eng. J.*, 2018, **354**, 407–431.
- 20 K. Zhu, J. Ou-Yang, Q. Zeng, S. Meng, W. Teng, Y. Song, S. Tang and Y. Cui, *Chin. J. Catal.*, 2020, **41**, 454–463.
- 21 S. B. Wang, B. Y. Guan and X. W. D. Lou, *J. Am. Chem. Soc.*, 2018, **140**, 5037–5040.
- 22 T. T. Hou, N. C. Luo, Y. T. Cui, J. M. Lu, L. Li, K. E. MacArthur, M. Heggen, R. T. Chen, F. T. Fan, W. M. Tian, S. Y. Jin and F. Wang, *Appl. Catal., B*, 2019, **245**, 262–270.
- 23 Y. Zhao, M. Wei, J. Lu, Z. L. Wang and X. Duan, *ACS Nano*, 2009, **3**, 4009–4016.
- 24 L. B. Staal, S. S. Charan Pushparaj, C. Forano, V. Prevot, D. B. Ravnsbæk, M. Bjerring and U. G. Nielsen, *J. Mater. Chem. A*, 2017, **5**, 21795–21806.
- 25 Z. Huang, P. Wu, B. Gong, Y. Fang and N. Zhu, *J. Mater. Chem. A*, 2014, **2**, 5534–5540.
- 26 Z. X. Chen, D. Z. Li, W. J. Zhang, C. Chen, W. J. Li, M. Sun, Y. H. He and X. Z. Fu, *Inorg. Chem.*, 2008, **47**, 9766–9772.
- 27 C. Tan, G. Zhu, M. Hojamberdiev, K. S. Lokesh, X. Luo, L. Jin, J. Zhou and P. Liu, *J. Hazard. Mater.*, 2014, **278**, 572–583.
- 28 Q. Liu, H. Lu, Z. Shi, F. Wu, J. Guo, K. Deng and L. Li, *ACS Appl. Mater. Interfaces*, 2014, **6**, 17200–17207.
- 29 L. Wei, Y. Chen, Y. Lin, H. Wu, R. Yuan and Z. Li, *Appl. Catal., B*, 2014, **144**, 521–527.
- 30 S. Li, L. Wang, Y. Li, L. Zhang, A. Wang, N. Xiao, Y. Gao, N. Li, W. Song, L. Ge and J. Liu, *Appl. Catal., B*, 2019, **254**, 145–155.
- 31 G. Ma, C. Shang, M. Jin, L. Shui, Q. Meng, Y. Zhang, Z. Zhang, H. Liao, M. Li, Z. Chen, M. Yuan, X. Wang, C. Wang and G. Zhou, *J. Mater. Chem. C*, 2020, **8**, 2693–2699.
- 32 J. S. Chen, F. Xin, H. L. Niu, C. J. Mao and J. M. Song, *Mater. Lett.*, 2017, **198**, 1–3.
- 33 M. Zhou, S. B. Wang, P. J. Yang, Z. S. Luo, R. S. Yuan, A. M. Asiri, M. Wakeel and X. C. Wang, *Chem. – Eur. J.*, 2018, **24**, 18529–18534.
- 34 J. L. Lin, Z. M. Pan and X. C. Wang, *ACS Sustainable Chem. Eng.*, 2014, **2**, 353–358.
- 35 H. Liu, J. Zhang and D. Ao, *Appl. Catal., B*, 2018, **221**, 433–442.
- 36 B. Lin, H. Li, H. An, W. B. Hao, J. J. Wei, Y. Z. Dai, C. S. Ma and G. D. Yang, *Appl. Catal., B*, 2018, **220**, 542–552.
- 37 L. C. Grabow and M. Mavrikakis, *ACS Catal.*, 2011, **1**, 365–384.
- 38 L. Liang, X. Li, Y. Sun, Y. Tan, X. Jiao, H. Ju, Z. Qi, J. Zhu and Y. Xie, *Joule*, 2018, **2**, 1004–1016.
- 39 Y. Zhao, G. Chen, T. Bian, C. Zhou, G. I. N. Waterhouse, L.-Z. Wu, C.-H. Tung, L. J. Smith, D. O'Hare and T. Zhang, *Adv. Mater.*, 2015, **27**, 7824–7831.